



HAL
open science

Characterization of the Gamma-ray Emission from the Kepler Supernova Remnant with Fermi-LAT

F. Acero, M. Lemoine-Goumard, J. Ballet

► **To cite this version:**

F. Acero, M. Lemoine-Goumard, J. Ballet. Characterization of the Gamma-ray Emission from the Kepler Supernova Remnant with Fermi-LAT. *Astronomy and Astrophysics - A&A*, 2022, 660, pp.A129. 10.1051/0004-6361/202142200 . hal-03655723

HAL Id: hal-03655723

<https://hal.science/hal-03655723v1>

Submitted on 29 Apr 2022

HAL is a multi-disciplinary open access archive for the deposit and dissemination of scientific research documents, whether they are published or not. The documents may come from teaching and research institutions in France or abroad, or from public or private research centers.

L'archive ouverte pluridisciplinaire **HAL**, est destinée au dépôt et à la diffusion de documents scientifiques de niveau recherche, publiés ou non, émanant des établissements d'enseignement et de recherche français ou étrangers, des laboratoires publics ou privés.

Characterization of the gamma-ray emission from the *Kepler* supernova remnant with *Fermi*-LAT

F. Acero¹, M. Lemoine-Goumard², and J. Ballet¹

¹ AIM, CEA, CNRS, Université Paris-Saclay, Université de Paris, 91191 Gif-sur-Yvette, France
e-mail: fabio.acero@cea.fr

² Univ. Bordeaux, CNRS, LP2I Bordeaux, UMR 5797, 33170 Gradignan, France

Received 10 September 2021 / Accepted 8 January 2022

ABSTRACT

The *Kepler* supernova remnant (SNR) had been the only historic SNR that lacked a detection at GeV and TeV energies, which probe particle acceleration. A recent analysis of *Fermi*-LAT data reported a likely GeV γ -ray candidate in the direction of the SNR. Using approximately the same data set but with an optimized analysis configuration, we confirm the γ -ray candidate to a solid $>6\sigma$ detection and report a spectral index of $2.14 \pm 0.12_{\text{stat}} \pm 0.15_{\text{sys}}$ for an energy flux above 100 MeV of $(3.1 \pm 0.6_{\text{stat}} \pm 0.3_{\text{sys}}) \times 10^{-12}$ erg cm⁻² s⁻¹. The γ -ray excess is not significantly extended and is fully compatible with the radio, infrared, and X-ray spatial distribution of the SNR. We successfully characterized this multiwavelength emission with a model in which accelerated particles interact with the dense circumstellar material in the northwest portion of the SNR and radiate GeV γ rays through π° decay. The X-ray synchrotron and inverse-Compton emission mostly stem from the fast shocks in the southern regions with a magnetic field $B \sim 100$ μ G or higher. Depending on the exact magnetic field amplitude, the TeV γ -ray emission could arise from either the south region (inverse-Compton dominated) or the interaction region (π° decay dominated).

Key words. ISM: supernova remnants – cosmic rays – supernovae: individual: Kepler – acceleration of particles – shock waves

1. Introduction

The last Galactic supernova to be observed from Earth occurred on October 9, 1604, and a detailed report was produced by Johannes Kepler, whose name is now attached to the supernova and its remnant. The *Kepler* supernova remnant (SNR) is most certainly the remnant of a Type Ia explosion, but the large-scale asymmetry, with brighter emission toward the north from radio to X-rays (DeLaney et al. 2002; Cassam-Chenaï et al. 2004; Blair et al. 2007; Reynolds et al. 2007), has caused some confusion with a core collapse origin (see Vink 2017, for a review). This asymmetry is now thought to be associated with the circumstellar medium (CSM) from a runaway supernova progenitor system with significant mass loss prior to the explosion in a single degenerate scenario (e.g., Bandiera 1987; Burkey et al. 2013; Katsuda et al. 2015).

Estimates for the distance to the SNR range widely in the literature, from 3 to 7 kpc (e.g., Reynoso & Goss 1999; Sankrit et al. 2005; Katsuda et al. 2008). The measurement of the proper motion of Balmer-dominated filaments using the *Hubble* Space Telescope at a 10-yr interval combined with the independently derived shock velocity from spectroscopy ($H\alpha$ line width) provides the most robust estimation at $d = 5.1_{-0.7}^{+0.8}$ kpc (Sankrit et al. 2016). Throughout the paper we use a distance of 5 kpc and rescale the values from the literature (e.g., shock speed) to match this distance whenever possible.

In the X-ray band, the emission is dominated by thermal emission with strong lines, and in particular Fe lines, supporting a Type Ia origin (e.g., Cassam-Chenaï et al. 2004; Reynolds et al. 2007). Nonthermal emission from thin synchrotron-dominated filaments was later revealed by *Chandra* observations (Bamba et al. 2005; Reynolds et al. 2007). Proper motion studies of

these synchrotron rims (Vink 2008; Katsuda et al. 2008) show fast shocks, with velocities¹ ranging from ~ 2000 km s⁻¹ in the northern region to ~ 5000 km s⁻¹ in the south.

The slower velocities in the north are related to the higher CSM density in this direction. Measurement of the thickness of these filaments suggests a high magnetic field of 150–300 μ G if the width is energy loss limited (Bamba et al. 2005; Parizot et al. 2006).

Despite being one of the youngest SNRs in our Galaxy with high velocity shocks and signs of dense material and interaction, *Kepler* had been the only historic SNR without detected γ -ray emission. This has changed with the recent report by Xiang & Jiang (2021) of a $\sim 3.8\sigma$ detection² with the *Fermi*-LAT telescope in the direction of the *Kepler* SNR. In addition, the recent detection of TeV γ rays after a deep exposure with the H.E.S.S. telescopes (152 h; Prokhorov et al. 2021; H.E.S.S. Collaboration 2022) opens the window for a detailed γ -ray study of this young and historic SNR.

In this work we aim to transform the status of the *Fermi*-LAT discovery from likely candidate to solid detection by using a more sophisticated analysis with approximately the same data set (see Sect. 2). In addition to the modest significance, Xiang & Jiang (2021) find a slightly offset best-fit position from the SNR. We thus analyze in detail if this offset is statistically compatible with SNR morphology as realized by multiwavelength spatial templates. We conclude in Sect. 3 by modeling *Kepler*'s multiwavelength emission under the assumption that γ rays are emitted from the northern interacting region and synchrotron and

¹ Velocities were rescaled to a 5 kpc distance.

² Significance associated with a test statistics of 22.94 with four degrees of freedom.

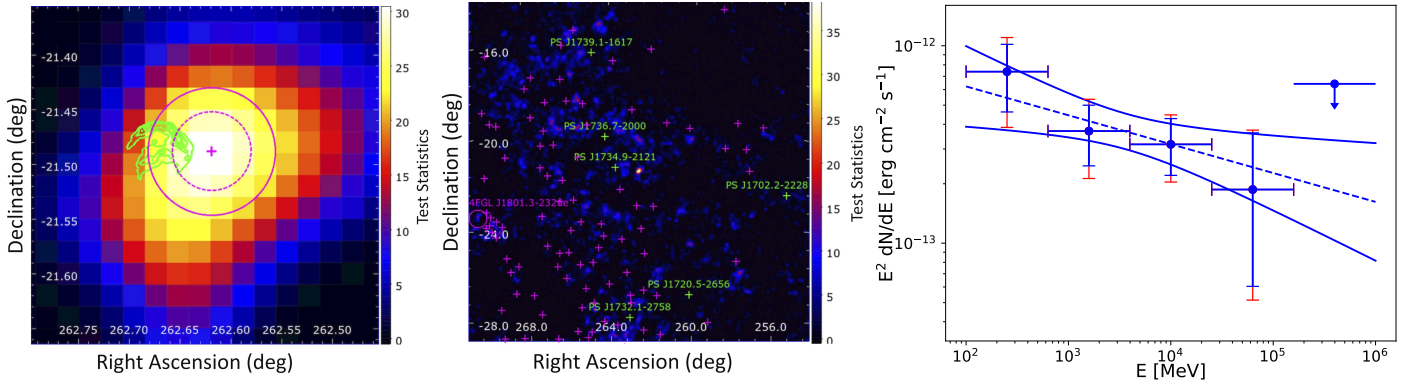


Fig. 1. Spatial and spectral characterization of the γ -ray emission results of *left panel*: zoomed-in view of the *Fermi*-LAT TS map at the *Kepler* SNR position above 1 GeV. The green contours are from the infrared 24 μm *Spitzer* map. The plus symbol and circles illustrate the best-fit position and the 68 and 95% confidence contours. *Middle panel*: *Fermi*-LAT TS map of the $15^\circ \times 15^\circ$ ROI around the *Kepler* SNR above 100 MeV. Magenta plus symbols represent the sources from the 4FGL-DR2 catalog and the green symbols the added point sources. For both TS maps, the *Kepler* SNR was not included in the model. *Right panel*: SED of the *Kepler* SNR obtained using the infrared spatial template. Blue error bars represent the statistical uncertainties, and the red ones correspond to the statistical and systematic uncertainties added in quadrature.

inverse-Compton emission arises mostly from the fast shocks in the southern region.

2. Analysis

2.1. LAT data reduction and preparation

The *Fermi*-LAT is a γ -ray telescope that detects photons via conversion into electron-positron pairs in the range from 20 MeV to higher than 500 GeV (Atwood et al. 2009). The following analysis was performed using 12 yr of *Fermi*-LAT data (2008 August 04 to 2020 August 03). A maximum zenith angle of 90° below 1 GeV and 105° above 1 GeV was applied to reduce the contamination of the Earth limb, and the time intervals during which the satellite passed through the South Atlantic Anomaly were excluded. Our data were also filtered, with time intervals around solar flares and bright γ -ray bursts removed. The data reduction and exposure calculations were performed using the LAT *fermitools* version 1.2.23 and *fermipy* (Wood et al. 2017) version 0.19.0. We performed a binned likelihood analysis and accounted for the effect of energy dispersion (when the reconstructed energy differs from the true energy) by using $\text{edisp_bins} = -3$. This means that the energy dispersion correction operates on the spectra with three extra bins below and above the threshold of the analysis³. Our binned analysis was performed with ten energy bins per decade, spatial bins of 0.02° for the morphological analysis and 0.05° for the spectral analysis over a region of $15^\circ \times 15^\circ$. We included all sources from the LAT 10-year Source Catalog (4FGL-DR2⁴) up to a distance of 15° from *Kepler*. Sources with a predicted number of counts below 1 and a significance of zero were removed from the model.

The summed likelihood method was used to simultaneously fit events with different angular reconstruction quality (PSF0 to PSF3 event types⁵). The Galactic diffuse emission was modeled by the standard file `gll_iem_v07.fits`, and the residual background and extragalactic radiation were described by a

single isotropic component with the spectral shape in the tabulated model `iso_P8R3_SOURCE_V3_v1.txt`. The models are available from the *Fermi* Science Support Center⁶.

Since the point spread function (PSF) of the *Fermi*-LAT is energy dependent and broad at low energy, we started the morphological analysis at 1 GeV. The spectral analysis was made from 100 MeV up to 1 TeV.

2.2. Morphological analysis

The spectral parameters of the sources in the model were first fit simultaneously with the Galactic and isotropic diffuse emissions from 1 GeV to 1 TeV. During this procedure, a point source fixed at the position ($\text{RA}_{J2000}, \text{Dec}_{J2000} = 262.62^\circ, -21.49^\circ$) reported by Xiang & Jiang (2021) was used to reproduce the γ -ray emission of the *Kepler* SNR. To search for additional sources in the region of interest (ROI), we computed a test statistic (TS) map that tests at each pixel the significance of a source with a generic E^{-2} spectrum against the null hypothesis $\text{TS} = 2(\ln \mathcal{L}_1 - \ln \mathcal{L}_0)$, where \mathcal{L}_0 and \mathcal{L}_1 are the likelihoods of the background (null hypothesis) and the hypothesis being tested (source plus background). We iteratively added four point sources in the model where the TS exceeded 25. We localized the four additional sources ($\text{RA}_{J2000}, \text{Dec}_{J2000} = 255.56^\circ, -22.47^\circ$; $260.13^\circ, -26.95^\circ$; $263.04^\circ, -27.97^\circ$; and $264.78^\circ, -16.30^\circ$), and we fit their power-law spectral parameters. We then localized the source associated with *Kepler* and obtained our best point source model at $\text{RA}_{J2000} = 262.618^\circ \pm 0.023^\circ$, $\text{Dec}_{J2000} = -21.488^\circ \pm 0.026^\circ$. The radii at 68% confidence and 95% confidence provided by *fermipy* are 0.036° and 0.058° . During this fit, we left free the normalization of sources located closer than 4° from the ROI center as well as the Galactic and isotropic diffuse emissions. Figure 1 (left panel) presents our best localization and confidence radii superimposed on the TS map above 1 GeV. We tested its extension by localizing a 2D symmetric Gaussian. The significance of the extension is calculated through $\text{TS}_{\text{ext}} = 2(\ln \mathcal{L}_{\text{ext}} - \ln \mathcal{L}_{\text{PS}})$, where \mathcal{L}_{ext} and \mathcal{L}_{PS} are the likelihood obtained with the extended and point source model, respectively. For *Kepler*, we found $\text{TS}_{\text{ext}} = 0.3$, which indicates that the emission is not significantly extended; this is compatible with the

³ https://fermi.gsfc.nasa.gov/ssc/data/analysis/documentation/Pass8_edisp_usage.html

⁴ https://fermi.gsfc.nasa.gov/ssc/data/access/lat/10yr_catalog

⁵ https://fermi.gsfc.nasa.gov/ssc/data/analysis/documentation/Cicerone/Cicerone_Data/LAT_DP.html

⁶ <https://fermi.gsfc.nasa.gov/ssc/data/access/lat/BackgroundModels.html>

Table 1. Results of the fit of the LAT data between 1 GeV and 1 TeV using different spatial models.

| Spatial model | TS | k | ΔAIC |
|-------------------|------|-----|--------------------|
| X-ray template | 28.6 | 2 | -24.6 |
| Radio template | 28.8 | 2 | -24.8 |
| Infrared template | 29.7 | 2 | -25.7 |
| Best point source | 32.1 | 4 | -24.1 |

Notes. The second column reports the TS values obtained for each spatial model, while Col. 3 indicates the number of degrees of freedom, k , adjusted in the model. The delta Akaike criterion is reported in the fourth column. See Sect. 2.2 for more details.

result from Xiang & Jiang (2021). The 95% confidence level upper limit on the extension is 0.09° (for comparison, the radius of the SNR is 0.03°).

Finally, we also examined the correlation of the γ -ray emission from *Kepler* with multiwavelength templates derived from the VLA at 1.4 GHz (DeLaney et al. 2002), *Spitzer* in the infrared at $24\ \mu\text{m}$ (Blair et al. 2007), and *Chandra* in the 0.5–4 keV energy band (Reynolds et al. 2007). We cannot use the likelihood ratio test to compare the hypothesis of a point source model to that of a multiwavelength template, because the two models are not nested. However, we can use the Akaike information criterion (AIC; Akaike 1974), which takes the number of independently adjusted parameters in a given model, k , into account. The standard AIC formula is $\text{AIC} = 2k - 2\ln \mathcal{L}$. Here we estimate a $\Delta\text{AIC} = 2k - \text{TS}$, comparing the AIC of the null source hypothesis and the AIC of the source being tested.

The lowest ΔAIC value, reported in Table 1, is obtained for the infrared template from *Spitzer*. While a lower ΔAIC indicates statistical preference for a model, the similar ΔAIC values indicate that each of these models provides an equally good representation of the γ -ray signal detected by the LAT. This result is consistent with our expectations from the *Fermi*-LAT PSF ($\sim 1^\circ$ at 1 GeV⁷) and the 0.03° SNR radius: all templates have a similar structure when convolved with the relatively broad PSF. Hence, in our analysis below, we adopt the infrared template but emphasize that any of these templates would yield similar residual TS maps or inferred spectral properties.

2.3. Spectral analysis

Using the best-fit infrared spatial template, we performed the spectral analysis from 100 MeV to 1 TeV. We first verified whether any additional sources were needed in the model by examining the TS maps above 100 MeV. Two additional sources were detected at $\text{RA}_{\text{J2000}}, \text{Dec}_{\text{J2000}} = 264.19^\circ, -20.01^\circ; 263.72^\circ, -21.36^\circ$ (not detected in the 1 GeV – 1 TeV range used in Sect. 2.2). The TS map obtained with all the sources considered in the model (see Fig. 1, middle panel) shows no significant residual emission, indicating that the ROI is adequately modeled. We then tested different spectral shapes for *Kepler*. During this procedure, the spectral parameters of sources located up to 4° from the ROI center were left free during the fit, like those of the Galactic and isotropic diffuse emissions. We tested a simple power-law model, a logarithmic parabola, and a smooth

Table 2. Impact on the source significance of different analysis setups above a 700 MeV energy threshold.

| Configuration number | Summed analysis | Bin size ($^\circ$) | Region size ($^\circ$) | TS |
|----------------------|-----------------|-----------------------|--------------------------|------|
| 1 | Yes | 0.05 | 15 | 33.9 |
| 2 | No | 0.05 | 15 | 30.6 |
| 3 | No | 0.1 | 15 | 23.2 |
| 4 | No | 0.1 | 20 | 21.4 |

Notes. For comparison, our setup corresponds to configuration 1 and that of Xiang & Jiang (2021) to configuration 4.

broken power-law model. Again, the improvement between the power-law model and the two other models was tested using the likelihood ratio test. In our case, ΔTS is 2.4 for the logarithmic parabola model and 3.1 for the smooth broken power-law representation, indicating that no significant curvature is detected. Assuming a power-law representation, the best-fit model for the photon distribution yields a TS of 38.3 above 100 MeV, a spectral index of $2.14 \pm 0.12_{\text{stat}} \pm 0.15_{\text{syst}}$, and a normalization of $(2.71 \pm 0.57_{\text{stat}} \pm 0.26_{\text{syst}}) \times 10^{-14} \text{ MeV}^{-1} \text{ cm}^{-2} \text{ s}^{-1}$ at the pivot energy of 2947 MeV. This implies an energy flux above 100 MeV of $(3.1 \pm 0.6_{\text{stat}} \pm 0.3_{\text{syst}}) \times 10^{-12} \text{ erg cm}^{-2} \text{ s}^{-1}$ and a corresponding γ -ray luminosity of $(0.93 \pm 0.18 \pm 0.09) \times 10^{34} \text{ erg s}^{-1}$ at a distance of 5 kpc.

The systematic errors on the spectral analysis depend on our uncertainties on the Galactic diffuse emission model, on the effective area, and on the spatial shape of the source. The first is calculated using eight alternative diffuse emission models following the same procedure as in the first *Fermi*-LAT SNR catalog (Acero et al. 2016) and the second is obtained by applying two scaling functions on the effective area. We also considered the impact on the spectral parameters when changing the spatial model from the infrared template to the best point source hypothesis. These three sources of systematic uncertainties were added in quadrature.

The *Fermi*-LAT spectral points shown in Fig. 1 (right panel) were obtained by dividing the 100 MeV–1 TeV energy range into five logarithmically spaced energy bins and performing a maximum likelihood spectral analysis to estimate the photon flux in each interval, assuming a power-law shape with fixed photon index $\Gamma = 2$ for the source. The normalizations of the diffuse Galactic and isotropic emission were left free in each energy bin, as were those of the sources within 4° . A 95% confidence level upper limit was computed when the TS value was lower than 1. Spectral data points are given in Table 3.

We examined the reason for the significant improvement of the derived TS value (of 38.3) with respect to the TS value of 22.9 above 700 MeV reported by Xiang & Jiang (2021). To do so, we reanalyzed the source above the same threshold, 700 MeV, using a point source localized at the position reported by Xiang & Jiang (2021). Their setup corresponds to configuration 4 in Table 2, and we find a TS value very similar to theirs (22.9). We tested several analyses with different spatial bin sizes, region sizes, and with or without the summed likelihood, and the improvement is shown step by step in Table 2. The higher TS value that we find in our analysis is most likely due to the summed likelihood analysis and the finer spatial binning of 0.05° (configuration 1). These improvements together with our lower energy threshold of 100 MeV boost our detection to the TS value of 38.3.

⁷ https://www.slac.stanford.edu/exp/glast/groups/canda/lat_Performance.htm

Table 3. *Fermi*-LAT flux data points using the infrared template.

| Energy band (GeV) | $E^2 dN/dE$ (10^{-13} erg cm $^{-2}$ s $^{-1}$) | TS |
|----------------------|--|-------|
| 0.25 (0.10–0.63) | 7.39 (2.77, –2.77) (2.19, –2.32) | 7.22 |
| 1.58 (0.63–3.98) | 3.70 (1.23, –1.30) (0.97, –1.03) | 9.72 |
| 10.00 (3.98–25.1) | 3.17 (0.96, –1.11) (0.59, –0.68) | 16.85 |
| 63.10 (25.1–158) | 1.87 (1.27, –1.75) (0.48, –0.65) | 4.44 |
| 398.11 (158–1000) | 6.41* | 0.65 |

Notes. The flux parameter with an asterisk denotes an upper limit. The first and second flux errors represent statistical and systematic errors, respectively.

3. Discussion

We next modeled the γ -ray emission in a multiwavelength context. As *Kepler* is a well-studied SNR, we aimed to build a coherent model by fixing as many parameters as possible from observations and theoretical grounds.

3.1. Model motivation

Our assumption is that, on the one hand, the observed GeV γ -ray emission is mostly of hadronic nature (π^0 decay) and is being radiated from the northwest hemisphere, where the shock is in interaction with the dense CSM as traced by infrared and optical maps. On the other hand, the leptonic components (synchrotron and inverse-Compton) arise from high velocity regions mostly observed in the south, with shock speed⁸ ranging from 4000–7000 km s $^{-1}$ (regions 4–12; Katsuda et al. 2008). X-ray synchrotron emission requires high-speed shock regions, but radio emission can be produced by slower shocks. However, for simplicity, we modeled the electron population with a single radio to X-ray population. Consequently, we expect our model will underpredict the radio data points.

We used the measured and inferred properties of the SNR to fix various parameters of our model. First, we fixed the fast shocks (leptonic components) at 5000 km s $^{-1}$ and the slower shocks in the interacting region at 1700 km s $^{-1}$ for a target density of 8 cm $^{-3}$ as reported in Sankrit et al. (2016). Secondly we derived the electron spectral distribution assuming that the electron maximal energy is limited by synchrotron losses and that proton maximal energy is limited by the age of the remnant.

3.2. Theoretical context

Following the prescription of Parizot et al. (2006), the acceleration timescale for the particles to reach an energy E at the forward shock can be written as

$$\tau_{\text{acc}} \simeq (30.6 \text{ yr}) \frac{3r^2}{16(r-1)} \times k_0(E) \times E_{\text{TeV}} B_{100}^{-1} V_{\text{sh},3}^{-2}, \quad (1)$$

where r is the compression ratio assumed at the shock, B_{100} the downstream magnetic field in units of 100 μG , and $V_{\text{sh},3}$ the shock speed in units of 1000 km s $^{-1}$. The deviation to Bohm diffusion is parametrized by $k_0 \geq 1$, defined as $D(E) = k_0 D_{\text{Bohm}}(E)$, where D_{Bohm} is the Bohm diffusion coefficient. At a value of one, the acceleration at the shock is the most efficient, and the maximal reachable energy decreases for higher values of k_0 .

⁸ Velocities were rescaled from a distance of 4–5 kpc to be consistent with our distance assumption.

In the loss-limited regime, the electron maximal energy can be obtained by equating the acceleration timescale, τ_{acc} , to the synchrotron loss time at the shock, giving

$$E_{e,\text{max}} \simeq (8.3 \text{ TeV}) \times \bar{f}(r) \times k_0^{-1/2} \times B_{100}^{-1/2} \times V_{\text{sh},3}, \quad (2)$$

where $\bar{f}(r) \equiv f(r)/f(4)$, with $f(r) = \sqrt{r-1}/r$.

The maximal proton energy is obtained by equating τ_{acc} from Eq. (1) with the age of the remnant of 400 yr, giving

$$E_{p,\text{max}} \simeq (13.1 \text{ TeV}) \times T_{400} \times \bar{f}^2(r) \times k_0^{-1} \times B_{100} V_{\text{sh},3}^2, \quad (3)$$

where T_{400} is the age of the remnant in units of 400 yr. For the magnetic fields considered in this modeling ($B \sim 100 \mu\text{G}$), the synchrotron cooling is non-negligible and is modeled with a broken power law, with E_{break} obtained by equating the age of the remnant and the synchrotron loss time downstream of the shock, giving

$$E_{\text{break}} \simeq (3.1 \text{ TeV}) \times T_{400} \times B_{100}^{-2}. \quad (4)$$

Because of the cooling and the cut at the maximum energy, the electron population is modeled as an exponentially cutoff broken power law, with a change in slope after E_{break} to $\Gamma_2 = \Gamma_1 + 1$.

Assuming that the synchrotron emission is limited by cooling, the acceleration efficiency parameter, k_0 , can be indirectly estimated by comparing the shock speed and the cutoff energy of the X-ray synchrotron spectrum using Eq. (34) of Zirakashvili & Aharonian (2007). Such a study was carried out by Tsuji et al. (2021) on a population of SNRs, including *Kepler*. For *Kepler*'s southeastern regions, where fast shocks are observed (Tsuji et al. 2021, reg 4–8 in Table 2), k_0 (their η) ranges from 2.0 to 3.2, which is equivalent to 3.1–5.0⁹ when rescaled to a distance of 5 kpc instead of 4 kpc. Given the measured values mentioned above, we decided to fix $k_0 = 3.4$ (the median value of the distribution) for our modeling for both the electron and proton populations (radiative model shown in Fig. 2).

The radiative models from the *naima* packages (Zabalza 2015) were used with the *Pythia8* parametrization of Kafexhiu et al. (2014) for the π^0 decay. For the inverse Compton, a far-infrared field ($T = 30 \text{ K}$, $U_{\text{ph}} = 1 \text{ eV cm}^{-3}$) was used in addition to the cosmic microwave background (Porter et al. 2006).

3.3. Multiwavelength data and spectral energy distribution

For the multiwavelength data presented in Fig. 2, we used the updated compilation of radio fluxes from Castelletti et al. (2021), the X-ray data from the Suzaku XIS + HXD instruments (covering the 3–10 keV and 15–30 keV band, Nagayoshi et al. 2021), and the H.E.S.S. flux points from Prokhorov et al. (2021); H.E.S.S. Collaboration (2022). The newly derived *Fermi*-LAT flux points using the infrared spatial template are presented (same as Fig. 1).

The resulting adjusted models, shown in Fig. 2, were obtained with only four free parameters, namely the downstream magnetic field, a unique spectral index for electrons and protons, and the associated energy budgets (see Table 4). The electron population spectral index and the amplitude of the magnetic field are correlated in the spectral energy distribution (SED) fitting. Motivated by theoretical expectations from recent kinetic

⁹ Velocity is derived from proper motion, which depends linearly on the distance, and η has a square dependence on shock speed (see Eq. (3) from Tsuji et al. 2021).

Table 4. Parameters obtained from the modeling of the SED in different scenarios.

| Scenario | B (μG) | n_0 (cm^{-3}) | $V_{\text{sh,e}}$ (km s^{-1}) | $V_{\text{sh,p}}$ (km s^{-1}) | $\Gamma_{e,1}/\Gamma_{e,2}$ | $E_{\text{break,e}}$ (TeV) | $E_{\text{max,e}}$ (TeV) | Γ_p | $E_{\text{max,p}}$ (TeV) | W_e (erg) | W_p (erg) |
|-----------------------------|--------------------------|-------------------------------|---|---|-----------------------------|-------------------------------|-----------------------------|------------|-----------------------------|----------------------|----------------------|
| High magnetic field | 170 | [8] | [5000] | [1700] | 2.2/[3.2] | [1.1] | [18.4] | 2.2 | [21.2] | 1.7×10^{47} | 5.6×10^{48} |
| Intermediate magnetic field | 90 | [8] | [5000] | [1700] | 2.3/[3.3] | [3.9] | [25.3] | 2.3 | [11.2] | 5.6×10^{47} | 5.6×10^{48} |

Notes. Parameters in brackets are fixed from observables or theory (see Sects. 3.1 and 3.2), while other parameters are adjusted to the data. The energy budget values are integrated above 1 GeV.

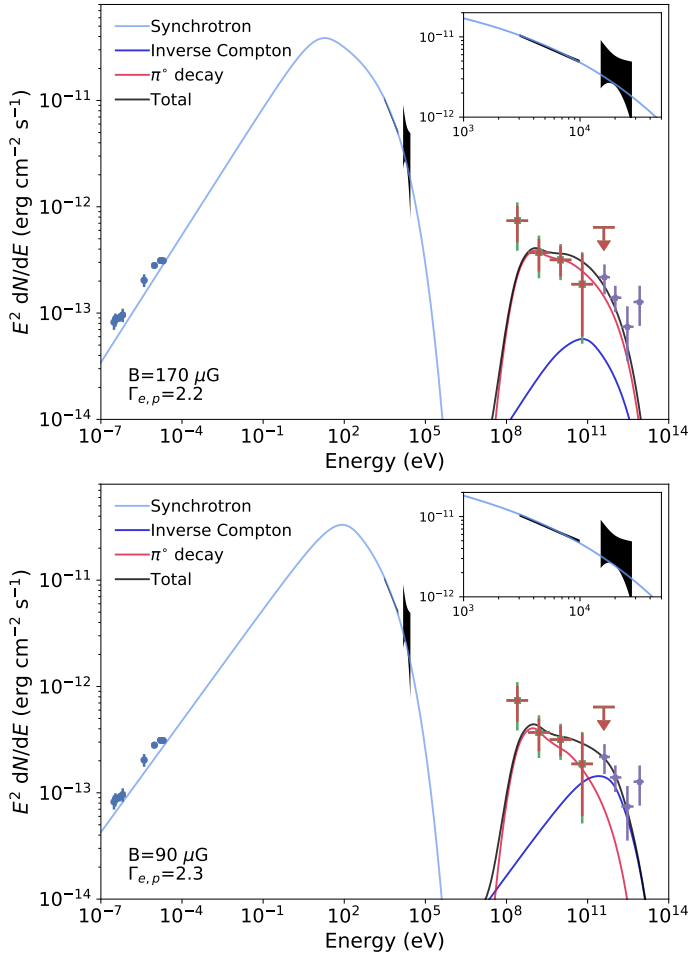


Fig. 2. Spectral energy modeling in an intermediate and high magnetic field scenario. The leptonic emission is assumed to arise from the fast shocks in the southern regions and the hadronic emission from the northwest interaction region. For the *Fermi*-LAT flux points, both the statistical errors and summed errors ($\sqrt{\text{stat}^2 + \text{syst}^2}$) are shown. Modeling parameters are listed in Table 4.

hybrid simulations (Diesing & Caprioli 2021) predicting spectral indices steeper than 2, we present two different scenarios for spectral indices of 2.3 and 2.2, corresponding to an intermediate (90 μG) and high magnetic field value (170 μG), respectively. A viable scenario, not shown in Fig. 2, can also be obtained for $B = 250 \mu\text{G}$ if the spectral index is changed to 2.15. Such a magnetic field value is compatible with the estimated values at the shock given the thin X-ray synchrotron filament size (Bamba et al. 2005; Rettig & Pohl 2012). When changing k_0 to 1 for the protons (i.e., maximal acceleration efficiency), $E_{p,\text{max}}$ increases

and slightly improves the model agreement with the H.E.S.S. flux points in the hadronic-dominated case.

Assuming that the hadronic emission arises from a small angular region in the SNR could explain the modest energy budget required (5.6×10^{48} erg). On the *Spitzer* infrared 24 μm images and the Hubble $H\alpha$ images from Sankrit et al. (2016), the northwest interacting region has an opening angle of $\sim 45^\circ$. Assuming a similar angle in the third dimension, this spherical cap represents $\sim 15\%$ of the SNR surface. The local proton energy budget is therefore equivalent to about 4% of the local kinetic energy, assuming an energy explosion of 10^{51} erg.

The intermediate and high magnetic field scenarios reproduce equally well the GeV to TeV flux points and cannot be disentangled from the SED analysis alone. However, we note that the inverse-Compton emission dominates above 300 GeV in an intermediate magnetic field case, while the hadronic emission dominates the entire γ -ray band for a high magnetic field scenario. Therefore, if the inverse-Compton emission arises from the fast moving shocks in the southern regions, the precise location of the TeV γ -ray emission might be able to constrain the hadronic or leptonic nature of the emission and, indirectly, the average magnetic field in the SNR. The distance between the dense interacting region in the northwest and the southern rim is on the order of 0.05° . While this is at the limit of the H.E.S.S. telescopes source localization precision for a faint source, a comparison of the GeV and TeV best-fit positions could shed light on the nature of TeV γ -ray emission. With an increased sensitivity and spatial resolution, the next-generation Cherenkov Telescope Array (Cherenkov Telescope Array Consortium 2019) will probe *Kepler's* γ -ray emission spatial distribution with greater accuracy and bring additional constraints on its nature.

3.4. *Kepler* SNR γ -ray emission in context

The detection of the *Kepler* SNR at GeV and TeV energies completes our high-energy view of historical SNRs. In this section we compare the global spectral properties of the young and likely hadronic-dominated SNRs *Kepler*, *Tycho*, and Cassiopeia A to those of the older middle-aged SNRs W 44, IC 443, and Cygnus Loop. We note that other young SNRs, such as SN 1006, RX J1713.7–3946, and RCW 86, which show a spectral slope $\Gamma \sim 1.5$ at GeV energies (see, e.g., Acero et al. 2015), are likely dominated by leptonic emission and are not considered in our sample. The distances to the sources are fixed to 3.33 ± 0.10 kpc for Cassiopeia A (Alarie et al. 2014), 4 ± 1 kpc for *Tycho* (Hayato et al. 2010), $5.1^{+0.8}_{-0.7}$ kpc for *Kepler* (Sankrit et al. 2016), 735 ± 25 pc for Cygnus Loop (Fesen et al. 2018), 3.0 ± 0.3 kpc for W 44 (Ranasinghe & Leahy 2018), and 1.7 ± 0.1 kpc for IC 443 (Yu et al. 2019).

Figure 3 compares the SED in terms of luminosity of the aforementioned SNRs. As a proxy to discuss spectral curvature, we estimated the hardness ratio $\text{HR} = \nu F_{1\text{TeV}}/\nu F_{1\text{GeV}}$.

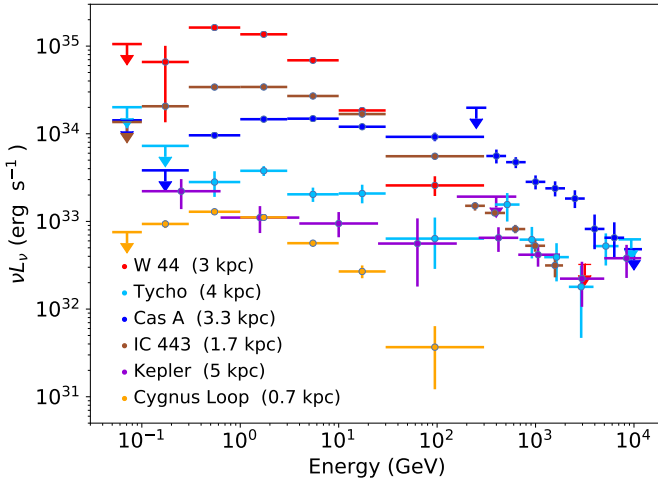


Fig. 3. Luminosity SEDs of a selection of SNRs for which the distance is well constrained and the γ -ray emission is likely dominated by hadronic emission. The *Fermi*-LAT data points are taken from the 4FGL DR2 catalog (Ajello et al. 2020) except for *Kepler*, where data from this work are used. TeV spectral data points for Cassiopeia A are taken from Abeysekara et al. (2020), from Archambault et al. (2017) for *Tycho*, from Prokhorov et al. (2021); H.E.S.S. Collaboration (2022) for *Kepler*, from Humensky & VERITAS Collaboration (2015) for IC 443, and from H.E.S.S. Collaboration (2018) for W44 (upper limit from the H.E.S.S. galactic plane survey). The references for the distances are given in the main text.

Tycho, *Kepler*, and Cassiopeia A exhibit a nearly flat spectrum ($HR = 0.2\text{--}0.4$), while the curvature is stronger for IC 443 ($HR = 0.015$) and W 44 ($<2 \times 10^{-3}$). Such a contrast is due to differences in the acceleration and emission mechanisms. In the young SNR sample, high shock speeds ($3000\text{--}6000 \text{ km s}^{-1}$) that produce highly energetic cosmic rays are observed; the cosmic rays interact with circumstellar material. The second sample exhibits lower shock speeds (few 100 km s^{-1}) with the presence of radiative shocks, where the compression and reacceleration of preexisting cosmic rays takes place, producing a spectral break at lower energies than for the young SNR sample. We note that the separation in terms of luminosity in our sample is not as clear. While W 44 is 50–100 times more luminous at 1 GeV than *Kepler* and *Tycho*, it is also 100 times more luminous than Cygnus Loop at 1 GeV. This is related to the fact that the shock in W 44 is interacting with dense molecular environments of a few 100 cm^{-3} (Yoshiike et al. 2013), whereas the environment’s density is closer to $\sim 1\text{--}10 \text{ cm}^{-3}$ in Cygnus Loop (Fesen et al. 2018).

4. Conclusion

By using ~ 12 yr of *Fermi*-LAT data and a summed likelihood analysis with the PSF event types, we were able to confirm GeV γ -ray emission at a $>6\sigma$ detection level that is spatially compatible with the *Kepler* SNR. From the analysis of this γ -ray emission, we draw the following conclusions:

- Above 100 MeV, the source is detected with a $TS = 38.3$ with a power-law index of $2.14 \pm 0.12_{\text{stat}} \pm 0.15_{\text{sys}}$.
- The source is not significantly extended, with an upper limit on its extension of 0.09° (SNR radius is 0.03°).
- The SED is modeled in a scenario with only four free parameters (B , $\Gamma_{e,p}$, W_e , and W_p), the rest being fixed using literature values and on theoretical grounds. The GeV γ -ray

emission is interpreted as π^0 decay from the northwest interaction region. The TeV emission could be inverse-Compton dominated ($B < 100 \mu\text{G}$; expected peak location in the south) or π^0 decay dominated ($B > 100 \mu\text{G}$; expected peak location in the northwest).

- Assuming a particle density of 8 cm^{-3} , derived from infrared observations, and that the interaction region represents 15% of the SNR surface, the local fraction of kinetic energy transferred to accelerated particles is on the order of 4%.

While this is at the limit of current generation instruments, a comparison of the *Fermi*-LAT and H.E.S.S. best-fit positions and errors could help to understand the dominant emission process at TeV energies. In addition, future observations with the Cherenkov Telescope Array will enable a detailed morphological analysis of the γ -ray emission and probe the high end of the γ -ray spectrum to test the maximal energies that this young particle accelerator can reach.

Acknowledgments. The authors would like to thank the *Fermi*-LAT internal referee Francesco de Palma and the journal referee for comments and suggestions that helped improve the clarity of the paper. F.A. would like to acknowledge the hospitality of Villa Port Magaud where part of this work was carried out. M.L.G. acknowledges support from Agence Nationale de la Recherche (grant ANR-17-CE31-0014). The *Fermi*-LAT Collaboration acknowledges generous ongoing support from a number of agencies and institutes that have supported both the development and the operation of the LAT as well as scientific data analysis. These include the National Aeronautics and Space Administration and the Department of Energy in the United States, the Commissariat à l’Énergie Atomique and the Centre National de la Recherche Scientifique/Institut National de Physique Nucléaire et de Physique des Particules in France, the Agenzia Spaziale Italiana and the Istituto Nazionale di Fisica Nucleare in Italy, the Ministry of Education, Culture, Sports, Science and Technology (MEXT), High Energy Accelerator Research Organization (KEK) and Japan Aerospace Exploration Agency (JAXA) in Japan, and the K. A. Wallenberg Foundation, the Swedish Research Council and the Swedish National Space Board in Sweden. Additional support for science analysis during the operations phase is gratefully acknowledged from the Istituto Nazionale di Astrofisica in Italy and the Centre National d’études Spatiales in France. Softwares: This research made use of *astropy*, a community-developed Python package for Astronomy (Astropy Collaboration 2013, 2018), of *fermipy* a Python package for the *Fermi*-LAT analysis (Wood et al. 2017), and of *gammapy*, a community-developed Python package for TeV gamma-ray astronomy (Deil et al. 2017). The *naima* package was used for the modeling (Zabalza 2015).

References

- Abeysekara, A. U., Archer, A., Benbow, W., et al. 2020, *ApJ*, 894, 51
 Acero, F., Lemoine-Goumard, M., Renaud, M., et al. 2015, *A&A*, 580, A74
 Acero, F., Ackermann, M., Ajello, M., et al. 2016, *ApJS*, 224, 8
 Ajello, M., Angioni, R., Axelsson, M., et al. 2020, *ApJ*, 892, 105
 Akaike, H. 1974, *IEEE Trans. Automat. Contr.*, 19, 716
 Alarie, A., Bilodeau, A., & Drissen, L. 2014, *MNRAS*, 441, 2996
 Archambault, S., Archer, A., Benbow, W., et al. 2017, *ApJ*, 836, 23
 Astropy Collaboration (Robitaille, T. P., et al.) 2013, *A&A*, 558, A33
 Astropy Collaboration (Price-Whelan, A. M., et al.) 2018, *AJ*, 156, 123
 Atwood, W. B., Abdo, A. A., Ackermann, M., et al. 2009, *ApJ*, 697, 1071
 Bamba, A., Yamazaki, R., Yoshida, T., Terasawa, T., & Koyama, K. 2005, *ApJ*, 621, 793
 Bandiera, R. 1987, *ApJ*, 319, 885
 Blair, W. P., Ghavamian, P., Long, K. S., et al. 2007, *ApJ*, 662, 998
 Burkey, M. T., Reynolds, S. P., Borkowski, K. J., & Blondin, J. M. 2013, *ApJ*, 764, 63
 Cassam-Chenaï, G., Decourchelle, A., Ballet, J., et al. 2004, *A&A*, 414, 545
 Castelletti, G., Supan, L., Peters, W. M., & Kassim, N. E. 2021, *A&A*, 653, A62
 Cherenkov Telescope Array Consortium (Acharya, B. S., et al.) 2019, *Science with the Cherenkov Telescope Array* (World Scientific Publishing Co. Pte. Ltd.)
 Deil, C., Zanin, R., Lefaucheur, J., et al. 2017, *Int. Cosmic Ray Conf.*, 301, 766
 DeLaney, T., Koralesky, B., Rudnick, L., & Dickel, J. R. 2002, *ApJ*, 580, 914
 Diesing, R., & Caprioli, D. 2021, *ApJ*, 922, 1
 Fesen, R. A., Weil, K. E., Cisneros, I. A., Blair, W. P., & Raymond, J. C. 2018, *MNRAS*, 481, 1786
 H.E.S.S. Collaboration (Abdalla, H., et al.) 2018, *A&A*, 612, A1

- H.E.S.S. Collaboration, Aharonian, F., Ait Benkhali, F et al. 2022, *A&A*, submitted [arXiv:2201.05839]
- Hayato, A., Yamaguchi, H., Tamagawa, T., et al. 2010, *ApJ*, 725, 894
- Humensky, B., & VERITAS Collaboration 2015, *Int. Cosmic Ray Confe.*, 34, 875
- Kafexhiu, E., Aharonian, F., Taylor, A. M., & Vila, G. S. 2014, *Phys. Rev. D*, 90, 123014
- Katsuda, S., Tsunemi, H., Uchida, H., & Kimura, M. 2008, *ApJ*, 689, 225
- Katsuda, S., Mori, K., Maeda, K., et al. 2015, *ApJ*, 808, 49
- Nagayoshi, T., Bamba, A., Katsuda, S., & Terada, Y. 2021, *PASJ*
- Nigro, C., Deil, C., Zanin, R., et al. 2019, *A&A*, 625, A10
- Parizot, E., Marcowith, A., Ballet, J., & Gallant, Y. A. 2006, *A&A*, 453, 387
- Porter, T. A., Moskalenko, I. V., & Strong, A. W. 2006, *ApJ*, 648, L29
- Prokhorov, D., Vink, J., Simoni, R., et al. 2021, Proceedings of the 37th International Cosmic Ray Conference (ICRC 2021) [arXiv:2107.11582]
- Ranasinghe, S., & Leahy, D. A. 2018, *AJ*, 155, 204
- Rettig, R., & Pohl, M. 2012, *A&A*, 545, A47
- Reynolds, S. P., Borkowski, K. J., Hwang, U., et al. 2007, *ApJ*, 668, L135
- Reynoso, E. M., & Goss, W. M. 1999, *AJ*, 118, 926
- Sankrit, R., Blair, W. P., Delaney, T., et al. 2005, *Adv. Space Res.*, 35, 1027
- Sankrit, R., Raymond, J. C., Blair, W. P., et al. 2016, *ApJ*, 817, 36
- Tsuji, N., Uchiyama, Y., Khangulyan, D., & Aharonian, F. 2021, *ApJ*, 907, 117
- Vink, J. 2008, *ApJ*, 689, 231
- Vink, J. 2017, *Handbook of Supernovae*, Supernova 1604, Kepler's Supernova and its Remnant (Berlin: Springer), 139
- Wood, M., Caputo, R., Charles, E., et al. 2017, *Int. Cosmic Ray Conf.*, 301, 824
- Xiang, Y., & Jiang, Z. 2021, *ApJ*, 908, 22
- Yoshiike, S., Fukuda, T., Sano, H., et al. 2013, *ApJ*, 768, 179
- Yu, B., Chen, B. Q., Jiang, B. W., & Zijlstra, A. 2019, *MNRAS*, 488, 3129
- Zabalza, V. 2015, *Int. Cosmic Ray Conf.*, 34, 922
- Zirakashvili, V. N., & Aharonian, F. 2007, *A&A*, 465, 695